REFLECTION LOSS-BASED ROADWAY WATER DEPTH MEASUREMENT FOR DRIVER SAFETY

Yi Geng[1] and Ting Zeng[2]
[1]CICT Mobile, Beijing 100085, China, [2]Beihang University, Beijing 100191, China

NOTE: Corresponding author: Yi Geng, gengyi@cictmobile.com

Abstract – *Flood fatalities generally occur in flood-prone areas such as low water bridges and tunnels, and most are vehicle-related. The existing water depth measurement solutions are neither cost-efficient nor suitable for roadway scenarios. This paper proposes two water depth measurement methods that can be integrated into cellular networks. The proposed methods reuse the periodic communication signals of 5G and 6G to avoid allocating dedicated sensing signals and conflicting with the communication requirements. The main idea of these methods is based on the fact that the Reflection Loss (RL) induced by a water surface exhibits a strong dependence on the water depth. The peak counting method measures the water depth by counting the successive RL peaks separated by a constant spacing. The RL fingerprinting method integrates the RL peak positions and the measured RL values to determine the water depth. Several factors affecting the water depth measurement resolution are also analyzed. The simulation results show that the measurable water depth range of the proposed methods is larger than the water depth that may pose danger to vehicles, indicating that the proposed methods are feasible for roadway scenarios.*

Keywords – Joint communications and sensing, reflection loss, sensor, water depth measurement, wireless systems

1. INTRODUCTION

There are numerous flood-prone areas on roads, mainly at low water bridges and tunnels. These flood-prone areas, which are easily flooded during or after heavy rainfall, pose immediate danger to the vehicles that try to cross during flooding conditions [1]. A report on flood fatalities indicates that over 50% of flooding deaths occur when the vehicles are driven into the hazardous flood waters [2]. Therefore, practical water depth measurement methods are required to improve the safety in these flood-prone areas.

A few technologies have been developed in recent decades to measure water depth. The most common and accurate way is a laser-based sensor, such as a lidar. The laser-based approaches determine the water depth by measuring the time difference of the laser beam reflected from the surface and the bottom of the water [3]. However, laser pulses may be affected by heavy rain because of the short wavelength of the laser. Furthermore, the cost and the power consumption of laser-based approaches are high. The ultrasonic sensor is another mature technology for water depth measurement [4]. Usually, ultrasonic sensors are attached to boats and submerged in water. Hence, it is not suitable for measuring the depth of the shallow water. From a hardware perspective, lidar and ultrasonic sensors for water depth measurements must work with communication networks to support water depth data transmission, inducing additional installation effort and cost. Moreover, none of the available technologies are suitable for a quick measurement of the water depth due to the latency between sensing and communication systems.

Joint Communications And Sensing (JCAS) is one of the prominent topics in 6G, utilizing the same spectral bands and the infrastructures for both sensing and communication purposes [5]. Usually, dense roadside Base Stations (BSs) have already been deployed for road traffic scenarios to achieve communication coverage. If the water depth measurement functionality can be built into the cellular network with ubiquitous BSs, it can rely on the large-scale infrastructure available almost everywhere. This paper proposes two Reflection Loss (RL)-based water depth measurement methods. The radio hardware and the communication signals are reused for roadway water depth measurement, achieving deep integration of communication and sensing services.

In terms of the structure, this paper starts with an overview of the existing material identification methods using communication infrastructures in Section 2, followed by a model of the reflection coefficient of the double-layer scatterer in Section 3. Section 4 gives a system model of RL-based water depth measurement. Sections 5 to 6 propose two water depth measurement methods based on the RL measurement. Section 7 discusses the resolution of the proposed methods and compares the proposed methods with the existing methods. Section 8 concludes the paper.

2. REFLECTION LOSS-BASED MATERIAL IDENTIFICATION

Using radio waves to identify the material of scatterers has been studied in detail in our previous work [6][7][8]. The general idea is based on the fact that the RL induced by a scatterer is a function of the scatterer's material
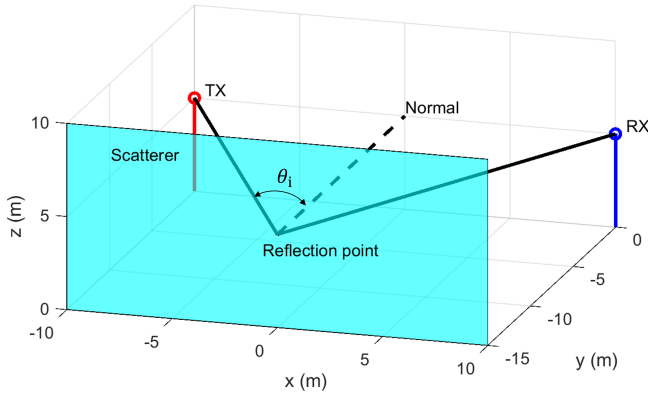
Fig. 1 – An illustration of how the RL is calculated
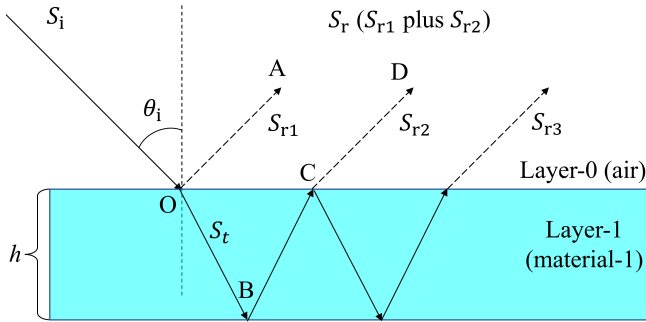
Fig. 2 – The transmit and reflected radio waves for an oblique radio wave S_i affected by a single-layer slab

properties, the incident angle, and the radio frequency. Therefore, the material of the scatterer can be estimated from the RL measurement. The implementation of the RL-based material identification is described as follows. As illustrated in Fig. 1, a radio wave transmitted by the transmitter (TX impinges on a scatterer at the reflection point with incident angle θ_i. The RL induced by the scatterer can be calculated by [6]

$$RL = P_{TX} - P_{RX} - FSPL \qquad (1)$$

where P_{TX} is the transmitted power at TX, P_{RX} is the received power at the receiver (RX), $FSPL$ is the free space path loss which can be calculated by Friis equation.

Our previous work [7] has derived the RL induced by a single-layer slab. Fig. 2 illustrates a radio wave S_i impinging on a thin slab made by a specific material at incident angle θ_i. For Transverse Electric (TE) polarization, the reflection coefficient induced by a single-layer slab r_{SL} can be calculated by
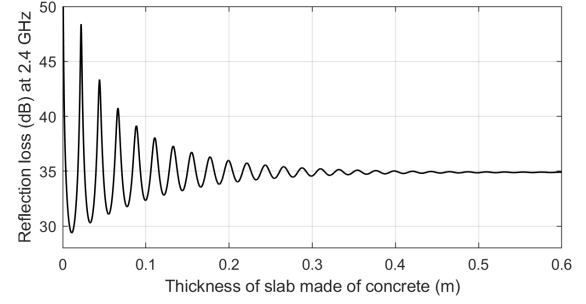
$$r_{SL} = \frac{r(1 - \exp(-j2q))}{1 - r^2 \exp(-j2q)} \qquad (2)$$

where

$$q = 2\pi h f \sqrt{\eta - \sin^2\theta_i} \qquad (3)$$

$$\eta = af^b - j17.98cf^d/f \qquad (4)$$

and h is the thickness of the slab, f is the frequency of the incident wave, η is the relative permittivity of the material and can be calculated by the material properties a, b,

Fig. 3 – The RL induced by a concrete slab at 2.4 GHz as a function of the slab thickness

c, and d [9]. r in Equation *(2)* represents the reflection coefficient when the slab is sufficiently thick, r is given by

$$r = \frac{\cos\theta_i - \sqrt{\eta - \sin^2\theta_i}}{\cos\theta_i + \sqrt{\eta - \sin^2\theta_i}} \qquad (5)$$

The reflection coefficient is the ratio of the reflected and incident wave amplitudes. We are more interested in reflection coefficient power R_{SL}, which is the square of the reflection coefficient:

$$R_{SL} = |r_{SL}|^2 \qquad (6)$$

By using equations *(2)-(6)*, the RL induced by a single-layer slab can be calculated by converting the reflection coefficient power R_{SL} in percentage terms into the RL in decibels. Fig. 3 gives an example of the RL for a concrete slab at 2.4 GHz with an incident angle of 45°, taking the material properties of concrete $a = 5.24$, $b = 0$, $c = 0.0462$, and $d = 0.7822$ [9]. It can be observed that the RL curve fluctuates less and less and converges to a fixed value as the slab thickness increases. The reason for this oscillation is that the wave reflected from the surface of the slab and the wave reflected from the bottom of the slab interfere with each other. As illustrated in Fig. 2, when an incident wave S_i impinges on the slab, both the reflection and transmission occur according to Snell's laws. The first-order reflected wave is denoted by S_{r1}. The transmitted wave S_t enters the slab, and S_t may be reflected and refracted multiple times in the slab, producing the second-order reflected wave S_{r2}, the third-order reflected wave S_{r3}, and so on. Usually S_{r3} is too weak, we consider S_{r1} and S_{r2} only. As the slab thickness h changes, the phase shifts between S_{r1} and S_{r2} also change. The amplitude of the reflected wave S_r, which is the interference result of S_{r1} and S_{r2}, depends on the slab thickness h. The constructive interference of S_{r1} and S_{r2} forms an S_r with a higher amplitude, the destructive interference of S_{r1} and S_{r2} forms an S_r with a lower amplitude. When the thickness h increases to 0.5 m, the transmitted wave S_t in the concrete layer suffers from the total internal attenuation and will not interfere the reflected wave. Therefore, the RL curve converges to a fixed value of 35 dB.

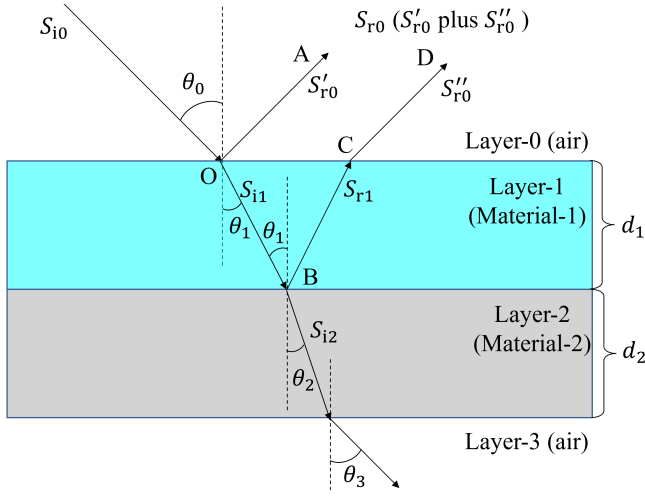## 3. REFLECTION COEFFICIENT MODEL OF DOUBLE-LAYER SCATTERER

Fig. 4 – The transmit and reflected radio waves for an oblique radio wave S_i affected by a double-layer slab

In this section, the RL induced by a double-layer slab is derived. Fig. 4 illustrates a scatterer consisting of two layers with smooth, parallel surfaces. Layer-1 is made of material-1 with a thickness of d_1, and Layer-2 is made of material-2 with a thickness of d_2. For the derivation purpose, we assume that the scatterer is in the air. The air from both sides of the scatterer is designated as Layer-0 and Layer-3 with the relative permittivity of 1 and the thickness of 0. The relative permittivity and the thickness of Layer-n (n= 0, 1, 2, and 3) are denoted by η_n and d_n, respectively. When a radio wave S_{i0} propagating in the air impinges on the scatterer with incident angle θ_0 at point O, S_{i0} is either reflected along OA as shown by S'_{r0} or refracted and transmitted in Layer-1 along OB as shown by S_{i1}. If Layer-1 is thin, the wave S_{i1} can penetrate Layer-1 and once again be either reflected by the bottom of Layer-2 along BC as shown by S_{r1} or refracted and transmitted in Layer-2 as shown by S_{i2}. S_{r1} may refract and emerge from the top surface of Layer-1 along CD as shown by S''_{r0}. S'_{r0} and S''_{r0} interfere with each other and produce a resultant wave S_{r0}. As explained in Section 2, the double-layer scatterer's reflection coefficient is dependent on the thickness of Layer-1.

The reflection coefficient for the scatterer consisting of two layers can be calculated by the following recursive method. Let θ_n denote the direction of the propagation in Layer-n. R_n and I_n denote the amplitude of the reflected wave and incident wave at the incident point on the surface of Layer-n, respectively. First initialize $R_3 = 1$ and $I_3 = 0$ for Layer-3. For n = 2, 1, 0,

$$I_n = \frac{1}{2}e^{\omega_n}[I_{n+1}(1+Y_{n+1}) + R_{n+1}(1-Y_{n+1})] \quad (7)$$

$$R_n = \frac{1}{2}e^{-\omega_n}[I_{n+1}(1-Y_{n+1}) + R_{n+1}(1+Y_{n+1})] \quad (8)$$

where

$$Y_{n+1} = \frac{\cos\theta_{n+1}}{\cos\theta_n}\sqrt{\frac{\eta_{n+1}}{\eta_n}} \quad (9)$$

$$\sin\theta_n = \frac{\sin\theta_0}{\sqrt{\eta_n}} \quad (10)$$

$$\omega_n = \frac{2\pi f}{c}\sqrt{\eta_n}d_n\cos\theta_n \quad (11)$$

$$\eta_n = a_n f^{b_n} - j17.98c_n f^{d_n}/f \quad (12)$$

and f is the frequency of the incident wave, c is the light speed, η_n is the relative permittivity of the material of Layer-n. a_n, b_n, c_n, and d_n are material properties of Layer-n that determine the relative permittivity and the conductivity of the material [9].

By calculating R_n and I_n in order $n = 2$ to $n = 0$, the reflection coefficient induced by the double-layer slab r_{DL} is given by

$$r_{DL} = \frac{R_0}{I_0} \quad (13)$$

## 4. SYSTEM MODEL OF RL-BASED WATER DEPTH MEASUREMENT

The JCAS systems can estimate the materials of the scatterers by measuring the RL induced by the scatterers [6]. On the contrary, the material information of the scatterers can be used to support, enable, and enrich the novel sensing use cases in cellular networks using the BSs as the sensors. This section presents the simulation setup and the system model for the RL-based water depth measurement.

The simulation is carried out in Matlab. First, we import the Three-Dimensional (3D) map for a low water bridge scenario in the Standard Tessellation Language (STL) format into Matlab. The STL format is a common 3D map format and can be converted from a variety of popular 3D software. There is a bridge deck layer and a water layer in the imported 3D map. The material of the bridge deck layer is specified as concrete. The thickness of the water layer can be configured to different values to simulate the water depth changes due to rainfall. Second, the configurations of two BSs in the 3D map are specified, including the carrier frequency, the position, the transmitted power, and the number of reflections for ray tracing analysis. Third, ray tracing analysis between the transmitting and receiving BS is performed using the shooting and bouncing method to compute the single-bounce reflection path. After detecting a single-bounce reflection path whose reflection point locates on the bridge deck, the position of the reflection point, the incident angle, and the overall path length can be obtained. Finally, we calculate the RL at the reflection point for different water depths with the result of ray tracing analysis.

Fig. 5 illustrates the simulated low water bridge scenario. The scenario shows a flood-prone area easily impacted by
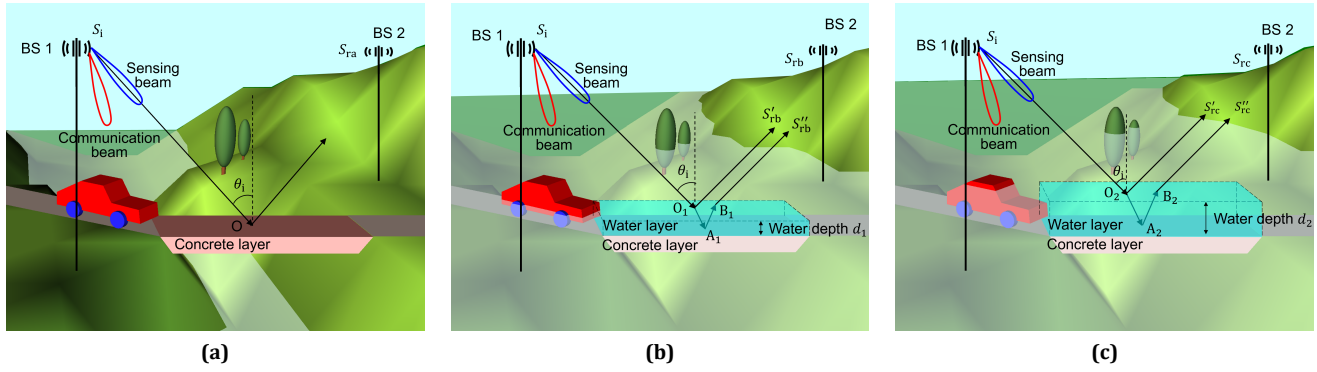
Fig. 5 – The illustration of a simulated low water bridge scenario: (a) the water level below the bridge surface (b) the flooded bridge with a water depth of d_1 (c) the flooded bridge with a water depth of d_2
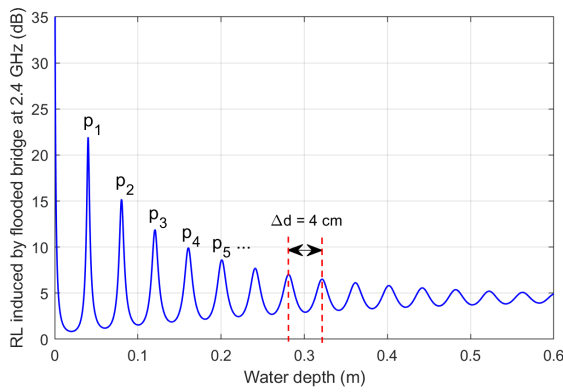
Fig. 6 – The RL induced by a flooded bridge as a function of the water depth at 2.4 GHz

rainfall and subsequent flood. The low water bridge provides the vehicular traffic when the water level is below the bridge surface, as shown in Fig. 5(a. The water level may rise above the bridge surface during or after heavy rainfall, as shown in Fig. 5(b. The rapidly rising water can even trap the vehicle and leads to the deaths of the people in the vehicle, as shown in Fig. 5(c.

We assume that the bridge deck in Fig. 5 is made of concrete. Two roadside BSs (BS 1 and BS 2 near the low water bridge deployed for the communication can also be used to measure the water depth on the bridge. BS 1 periodically transmits sensing signals for the water depth measurement at 2.4 GHz. At the beginning of the simulation, the water level is below the bridge surface, as shown in Fig. 5(a. The sensing signals are reflected by the bridge surface at point O at incident angle θ_i. Due to rainfall, the water depth on the bridge increased from 0 m to 0.6 m gradually. The incident angle θ_i is 45°. It is assumed that the water surface is perfectly calm. We also assume that the bridge deck is thick enough (e.g., 40 cm. Thus, the transmission wave in the concrete layer suffers from the total internal absorption and will not interfere with the reflected wave.

Fig. 6 illustrates the RL induced by the flooded bridge as

a function of the water depth when the concrete layer is significantly thick. The initial RL is 35 dB when the water depth is zero, which corresponds to the RL induced by the bridge deck made of concrete. The RL curve oscillates as the water depth increases, but the amplitude gradually decreases with the increasing water depth until eventually reaching a steady RL value of 5 dB. The oscillating behavior of the RL curve is caused by the additional propagation length Δl of the second-order reflected wave in the water layer, leading to the phase difference and interference between the first-order reflected wave and the second-order reflected wave. For example, in Fig. 5(b), water depth d_1 causes an additional propagation distance Δl ($O_1A_1 + A_1B_1$) of the second-order reflected wave S''_{rb} than the propagation distance of the first-order reflected wave S'_{rb}. Δl is given by

$$\Delta l = \frac{2d}{\cos\theta_t} = \frac{2d}{\cos(\arcsin(\frac{\sin\theta_i}{n_{water}}))} \qquad (14)$$

where θ_t is the refractive angle in the water. d is the water depth. n_{water} is the refractive index of water with a value of 1.33.

The first-order reflected wave and the second-order reflected wave are in phase when

$$\frac{\Delta l}{\lambda_{water}} = 0, 1, 2, \cdots \qquad (15)$$

and are half a cycle out of phase when

$$\frac{\Delta l}{\lambda_{water}} = \frac{1}{2}, \frac{3}{2}, \frac{5}{2}, \cdots \qquad (16)$$

where λ_{water} is the wavelength of the radio wave in the water.

From equations *(15)-(16)*, if the second-order wave propagates several integer cycles in the water layer, the first and second-order reflected wave will be in phase. The two waves create constructive interference, resulting in a reflected wave with a higher amplitude, corresponding to a peak in Fig. 6. If the second-order wave propagates
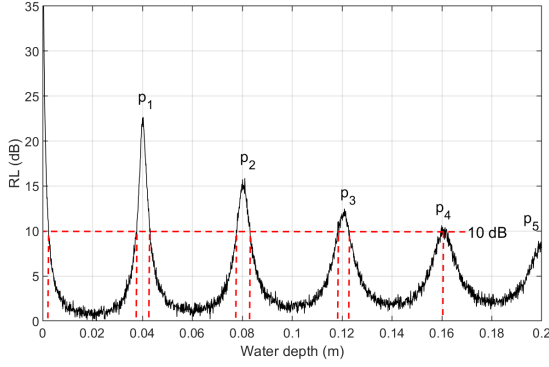
Fig. 7 – The RL with uncertainty induced by a flooded bridge as a function of the water depth
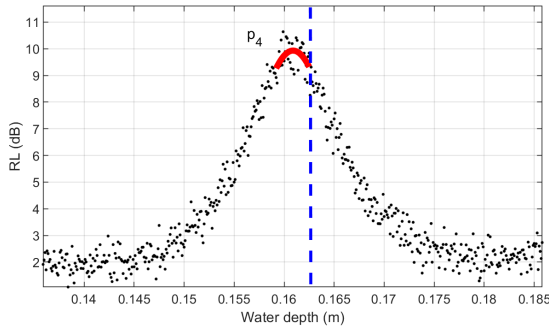
Fig. 8 – An illustration of how the RL peak is identified

several integer cycles and a half cycle in the water layer, the first and second-order reflected wave will be out of phase. The destructive interference of both the waves results in a reflected wave with a lower amplitude, which corresponds to a trough in Fig. 6. The alternating constructive interference and destructive interference due to the water depth changing create multiple peaks p_1, p_2, p_3, ⋯ along the RL curve as shown in Fig. 6.

According to equations *(14)-(16)*, the water depth difference between the successive peaks Δd is calculated to be 4 cm using the wavelength λ of 12.5 cm (the frequency of 2.4 GHz) and the incident angle θ_i of 45°. It is worth noting that when a radio wave travels from the air into the water, the wavelength of the wave in the water becomes shorter. For a radio wave at 2.4 GHz (λ = 12.5 cm), the wavelength in the water λ_{water} reduced to 9.4 cm. The calculation result of 4 cm accords closely with the simulation in Fig. 6. The peaks occur at the water depths 4 cm, 8 cm, 12 cm, and so on.

5. PEAK COUNTING METHOD

This section presents a novel RL-based water depth measurement method. The results of the water depth measurement methods can provide timely and adequate warning to approaching drivers that the flooded roadway conditions exist further up the road. The analysis in Section 4 shows a constant water depth difference Δd between the successive RL peaks due to water depth changing, which can be used to develop water depth measure-

ment solutions. Fig. 7 depicts the simulated RL measurements with uncertainty by corrupting the RL data with the white noise with zero-mean and 0.2 mean amplitude variance. At the beginning of the simulation, the water depth is zero, the concrete bridge deck induces a steady RL of 35 dB. Increasing the water depth on the bridge results in RL fluctuations. When the first RL peak p_1 is identified, the water depth is 4 cm. Similarly, the second peak p_2 corresponds to a water depth of 8 cm. Therefore, the critical problems of RL-based water depth solutions are to process RL measurement data and identify RL peaks that indicate the specific water depths.

One way to identify RL peaks is to use the fact that the first derivative of a peak has a downward-going zero-crossing at the peak maximum [10]. But the random noise and the measurement uncertainty in the real RL data will cause false peak detection. To avoid false peak detection, a so-called peak finding method first smooths the first derivative of the RL measurement data before looking for the downward-going zero-crossings. Then it takes only those zero-crossings whose slopes exceed a predefined "slope threshold" at a point where the original RL measurement exceeds an "amplitude threshold". The slope threshold is taken to indicate the peaks, then any peaks with a height less than the amplitude threshold are ignored. The peaks along the RL curve can be identified by tuning the value of the slope threshold and the amplitude threshold. Fig. 8 illustrates how the peak p_4 in Fig. 7 is identified. Each black dot in Fig. 8 presents an RL measurement at a specific water depth. The red curve segment is the smoothed RL data near peak p_4. When the water depth increases to 16.2 cm, where the dashed blue line indicates, both the slope threshold and the amplitude threshold are fulfilled, then the peak p_4 indicating a water depth of 16 cm can be identified.

6. RL FINGERPRINTING METHOD

The peak counting method is based on RL measurements of the frequent transmissions of the always-on sensing signals. When the water depth increases from zero (the dry roadway) due to rainfall, the RL induced by the roadway fluctuates due to the water depth changing. The water depth on the road can be estimated by counting the number of RL peaks. However, this always-on mode of the sensing signals reduces the network's power efficiency and increases the interference.

An on-demand transmission mode should also be supported to reduce the sensing overhead and power consumption. Only if the vehicles approach the low water bridge are the sensing signals transmitted by the roadside BSs. But the bridge may have already been flooded when transmitting the sensing signals. Hence, we cannot determine the water depth by counting the peaks since the peak indices are uncertain when the peak counting method is not implemented from the zero water depth.

Table 1 – A fingerprint database including the RL values at p_1-p_7

| Water depth in centimeters	4	8	12	16	20	24	28
Peak index	p_1	p_2	p_3	p_4	p_5	p_6	p_7
RL (dB)	21.9	15.2	11.9	9.9	8.6	7.7	7

For example, a vehicle sends a water depth measurement request to the JCAS system when it approaches a flooded low water bridge. The BS begins to transmit the sensing signals, and we assume that an RL of 10 dB has been measured. However, multiple water depths can induce an RL of 10 dB, and they are given with the red dashed lines in Fig. 7. Shortly afterward, an RL peak is identified due to the water depth changing using the peak finding method. But this peak can be any of p_1, p_2, p_3, and p_4. Therefore, the water depth cannot be determined.

In this section, we propose another RL-based water depth measurement method, the RL fingerprinting method. The RL fingerprinting method combines the peak finding method with the RL values at each identified peak to determine a unique water depth. The fingerprinting method consists of two phases, the RL data collecting phase and the RL matching phase. In the RL data collecting phase, an RL value is measured at each water depth inducing an RL peak, called a fingerprint. The measured RL data is stored in a fingerprint database along with their water depths. A fingerprint database including the RL values at p_1 to p_7 is tabulated in Table 1. In the RL matching phase, when an RL peak is identified, the measured RL at the peak is compared with the values stored in the database to infer the water depth. For instance, an RL of 15.2 dB measured at an RL peak indicates that the water depth is 8 cm.

Note that the amplitude of RL oscillation gradually decreases with increasing water depth. Therefore, when the water depth is high, the slight RL difference between the adjacent peaks makes it hard to distinguish between two RL values when they are close. Hence, the RL measurement uncertainty limits the measurable water depth range. According to Fig. 6, there are still significant fluctuations of the RL peaks at a water depth up to 40 cm. Twenty centimeters of water will reach the bottom of most passenger cars, causing loss of control and stalling [**11**]. Therefore, the measurable water depth range is more extensive than the water depth that may pose a danger to vehicles. The proposed method is feasible for roadway water depth detection.

7. DISCUSSIONS

The water depth measurement resolution of the proposed methods relies on the water depth difference Δd between the successive peaks of the RL curve. According to Equation *(14)*, the shorter wavelength allows a finer granularity in the propagation distance Δl (more wavelengths in Δl). Therefore, a finer granularity of water depth d can be obtained. Hence the higher frequencies with short
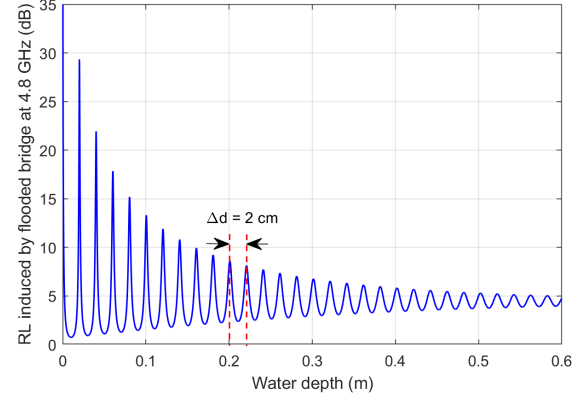
Fig. 9 – The RL induced by a flooded bridge as a function of the water depth at 4.8 GHz

wavelengths can provide the high-resolution water depth measurement. Fig. 9 depicts the RL induced by a flooded bridge with all parameters remaining the same as those in Fig. 6, except the frequency increases to 4.8 GHz. One can see that the resolution of water depth measurement Δd is improved to 2 cm simply because of the shorter wave- length at the higher frequencies.

Another way to increase the water depth measurement resolution is to use a larger incident angle θ_i. We assume that the water layers with the depths d_1 and d_2 in Fig. 5(b) and Fig. 5(c) induce the adjacent RL peaks, which means that the water depth measurement resolution Δd is equal to $d_2 - d_1$. The additional propagation distances in the water layer in Fig. 5(b) and Fig. 5(c) are defined as

$$\Delta l_1 = O_1 A_1 + A_1 B_1 \qquad (17)$$

$$\Delta l_2 = O_2 A_2 + A_2 B_2 \qquad (18)$$

According to geometry, Δl_1 and Δl_2 are given by

$$\Delta l_1 = \frac{2d_1}{\cos\theta_t} \qquad (19)$$

$$\Delta l_2 = \frac{2d_2}{\cos\theta_t} \qquad (20)$$

Δl_2 contains one more integer cycle (one wavelength in water λ_{water}) than that of Δl_1,

$$\lambda_{\text{water}} = \Delta l_2 - \Delta l_1 \qquad (21)$$

The water depth measurement resolution Δd is calculated from equations *(17)-(21)*, yielding

$$\Delta d = \frac{\lambda_{\text{water}}\cos\theta_t}{2} \qquad (22)$$

Table 2 – A comparison of different water depth sensing methods

KPI	RL-based method	Lidar	Ultrasonic sensor
Cost	Very low	Very high	High
Installation	N/A	Attach to vehicles	Attach to boats
Structure	Highly integrated	Independent system	Independent system
Measurement range	0 to 0.5 m	0 to 2.5 m	0.2 to 150 m
Accuracy	Centimeter-level	Millimeter-level	Decimeter-level
latency	Low	High	High
Robustness	High	Low (avoid bad weather)	High

The refractive angle θ_t in water is proportional to the incident angle θ_i in air. From Equation *(22)*, we can conclude that a larger incident angle θ_i induces a finer water depth measurement resolution Δd. But the incident angle θ_i cannot be too large to avoid the total reflection of the second-order wave in the water layer.

In practice, the water surface is not calm. The wind, raindrops, and vehicles ripple the water surface. The water surface waves will significantly complicate the reflection coefficient model of the double-layer scatterer. A low-band spectrum can make the water depth measurement methods more robust to the water surface waves. For example, a JCAS system operating at 700 MHz can tolerate the water waves because of its large wavelength of 43 cm, but with the cost of a lower water depth measurement resolution of 13 cm. Moreover, the roads in the real world may not be ideally as homogeneous as the materials modelled in [**9**]. For example, the road could be constructed of multiple layers and mixed materials. However, if the JCAS system measures the RL at a fixed point on the road during the RL data collecting phase and the RL matching phase, we need not know the model of the complex structures and can still obtain the water depth using the proposed methods.

According to Equation *(5)*, the RL is dependent only on the material properties, the incident angle, and the carrier frequency but independent of the signal properties such as transmitted power and bandwidth. The RX can calculate the RL using Equation *(1)* by performing the received power measurements as long as the RX knows P_{TX}, no matter what the communication signal is and what the transmitted power is. Therefore, many periodic signals of 5G NR, such as Synchronization Signal Block (SSB), Channel State Information Reference Signals (CSI-RS), and Positioning Reference Signal (PRS), can be reused for the water depth measurement to avoid allocating dedicated sensing signals and conflicting with the communication requirements.

A comparison of different water depth sensing methods is provided in Table 2. It can be seen from the table that the proposed method has the advantages of low cost, low latency, and high integration with the communication systems. Despite its short measurement range and lower accuracy, the proposed method is much more suitable than the lidar method or the ultrasonic sensor method for roadway scenarios because the water depth measurement for vehicles does not require high accuracy and a large measurement range.

8. CONCLUSION

In this paper, we propose two RL-based water depth measurement methods, which can become an integral part of the JCAS network. The proposed methods reuse the communication signals to avoid allocating dedicated sensing signals and degrading the communication performance. Using the ubiquitous BSs, the real-time water depth information can be provided to improve safety in flood-prone areas. This paper also discusses using the double-layer scatterer's reflection coefficient model to calculate the RL. Additionally, the paper explains ways to improve the water depth measurement resolution of the proposed methods. The simulation results show that the proposed methods provide the centimeter-level water depth measurement resolution and a large enough measurable range to support the vehicle-related water depth detection requests.

ACKNOWLEDGEMENT

REFERENCES

[1] H. Sharif and S. Dessouky "Portable Roadway High Water Detection System for Driver Safety and Infrastructure Assessment," University of Texas, San Antonio, USA, Aug. 2019.

[2] "National Weather Service (NWS), 2019: Flood fatalities," Hydrologic Information Center, USA, Apr. 2019.

[3] K. Shen et al., "Laser-based water depth measurement system deployed via unmanned aerial vehicle," J. Appl. Remote Sens, vol. 11, no. 3, Jun. 2017, doi: 10.1117/1.JRS.11.032409.

[4] S. Hajjaj, M. Sultan, M. Moktar and S. Lee, "Utilizing the Internet of Things (IoT) to Develop a Remotely

Monitored Autonomous Floodgate for Water Management and Control," J. Water, vol. 12, no. 502, Feb. 2020, doi: 10.3390/w12020502.

[5] H. Wymeersch et al., "Deliverable D3.1 Localisation and sensing use cases and gap analysis," Hexa-X, Dec. 31, 2021.

[6] Y. Geng, V. Yajnanarayana, A. Behravan, E. Dahlman and D. Shrestha, "Study of Reflection-Lass-Based Material Identification from Common Building Surfaces," 2021 Joint European Conference on Networks and Communications & 6G Summit (EuCNC/6G Summit), 2021, pp. 526-531, doi: 10.1109/EuCNC/6GSummit51104.2021.9482524.

[7] Y. Geng, "Map-Assisted Material Identification at 100 GHz and Above Using Radio Access Technology," 2022 Joint European Conference on Networks and Communications & 6G Summit (EuCNC/6G Summit), 2022, pp. 476-481, doi: 10.1109/EuCNC/6GSummit54941.2022.9815822.

[8] Y. Geng, D. Shrestha, V. Yajnanarayana, E. Dahlman, and A. Behravan, "Joint scatterer localization and material identification using radio access technology," J Wireless Com Network 2022, 87(2022), https://doi.org/10.1186/s13638-022-02167-7.

[9] Recommendation ITU-R P.2040-2, Effects of building materials and structures on radiowave propagation above about 100 MHz, International Telecommunications Union, Sep. 2021.

[10] T. O'Haver, "An introduction to signal processing in chemical measurement," J. Chemical Education, Jun. 1991, doi: 10.1021/ed068pA147.

[11] "Are You Ready? An In-Depth Guide to Citizen Preparedness," Federal Emergency Management Agency (FEMA), USA, Apr. 2019.

AUTHORS

Yi Geng received a B.S. degree from Shandong University, Jinan, China, in 2000, and an M.S. degree from Nanjing University of Posts and Telecommunications, Nanjing, China, in 2007. He has worked on research, development, rollout, and customer support of 2G, 3G, 4G, 5G, 6G mobile networks since 2007. He is currently a researcher in the field of 6G JCAS at CICT Mobile, China. His research interests include JCAS and aerial communications.

Ting Zeng received a B.S. degree and an M.S. degree from Beijing University of Posts and Telecommunications, Beijing, China, in 2018 and 2021, respectively. She is currently a PhD student at Beihang University, Beijing, China, a researcher in the field of 6G JCAS at CICT Mobile, China. Her research interests include JCAS and metasurface.